PHYSICAL REVIEW B **80**, 064504 (2009)

$BaPtSi_3$: A noncentrosymmetric BCS-like superconductor

E. Bauer, R. T. Khan, H. Michor, and E. Royanian
Institute of Solid State Physics, Vienna University of Technology, A-1040 Wien, Austria

A. Grytsiv, N. Melnychenko-Koblyuk, P. Rogl, D. Reith, and R. Podloucky
Institute of Physical Chemistry, University of Vienna, A-1090 Wien, Austria

E.-W. Scheidt
Chemische Physik und Materialwissenschaften, Universität Augsburg, D-86159 Augsburg, Germany

W. Wolf
Materials Design s.a.r.l., 44 Avenue F.-A. Bertholdi, 72000 Le Mans, France

M. Marsman
Department of Computational Materials Physics, Faculty of Physics, University of Vienna, A-1090 Wien, Austria
(Received 7 April 2009; revised manuscript received 15 July 2009; published 10 August 2009)

By investigations of phase relations in the alloy system Ba-Pt-Si at 900 °C we observe the formation of the compound $BaPtSi_3$, which crystallizes in the noncentrosymmetric $BaNiSn_3$ structure type. Its space group is $I4mm$ with the tetragonal lattice parameters $a=0.44094(2)$nm and $c=1.0013(2)$nm for the arc-melted compound annealed at 900 °C. The characterization of the physical properties of $BaPtSi_3$ reveals a superconducting transition at 2.25 K with an upper critical field at $T=0$ K of ≈ 0.05 T. For analyzing the electronic structure, density-functional theory calculations are performed yielding very good agreement between theory and experiment for the structural properties. From relativistic electronic-structure calculations, Fermi surface nesting features are found for two characteristic double sets of bands. The spin-orbit splitting of the relativistic electronic bands is in general rather small at Fermi energy and, therefore, superconductivity adheres to an almost undisturbed BCS state.

DOI: 10.1103/PhysRevB.80.064504 PACS number(s): 74.25.Bt, 74.70.Ad, 72.15.Eb

I. INTRODUCTION

The discovery of $CePt_3Si$ ($CePt_3B$-type structure) as the first heavy fermion superconductor without inversion symmetry[1] has initiated widespread research activities in the field of unconventional superconductors. Whereas $CePt_3Si$ shows superconductivity already at ambient pressure, a transition into a superconducting ground state of the few further examples of this type, UIr,[2] $CeRhSi_3$,[3] and $CeIrSi_3$ (Ref. 4) was found only at applied hydrostatic pressures of 10–20 kbar.

Noncentrosymmetry (NCS) introduces an electrical field gradient in the crystal and, thereby, creates a Rashba-type antisymmetric spin-orbit coupling.[5] An inherent feature is then the mixing of spin-singlet and spin-triplet Cooper-pairing channels which are otherwise distinguished by parity.[5] This mixing of pairing states is expected to cause a two-component order parameter.

Apart from heavy fermion properties, the occurrence of superconductivity in materials without inversion symmetry deserves its own merit. Therefore, we aim to find NCS superconducting materials without strong correlations among d or f electrons. This may set the stage for reliable electronic-structure calculations, proving the splitting of bands due to missing inversion symmetry. Previous examples of superconductors without strong electron correlation, where, however, NCS was not a central issue of investigation, are binary R_2C_{3-y} with R=La or Y,[6–8] or $Cd_2Re_2O_7$ with $T_c \approx 1$ K.[9,10]

More recently the solid solution $Li_2(Pd,Pt)_3B$ was demonstrated to show superconductivity.[11,12] While Li_2Pd_3B is accounted for in terms of a conventional BCS-like superconductor, Li_2Pt_3B refers to unconventionality[12–14] presumably due to a very large spin-orbit coupling.[15] A recent study on $Li_2Pd_xPt_{3-x}B$ by muon-spin rotation and specific heat, however, suggests that the whole series comprises single-gap s-wave superconductivity.[16] The complex metallic alloy Mg_2Al_3 also exhibits superconductivity in absence of inversion symmetry.[17]

In a detailed investigation of phase relations of the system Ba-Pt-Si at 900 °C,[18] the compound $BaPtSi_3$ was identified as a representative of the noncentrosymmetric $BaNiSn_3$ type exhibiting a phase transition to a superconducting state below 2 K. The present study aims to analyze and understand the superconducting properties of $BaPtSi_3$ by deriving the electronic structure from density-functional theory calculations in order to demonstrate the antisymmetric, Rashba-type spin-orbit coupling.

II. EXPERIMENTAL

Alloys of $BaPtSi_3$ with a weight of about 1.5 g were prepared by arc melting on a water-cooled copper hearth in Ti-gettered argon from elemental ingots with a minimal purity of 99.9 mass%. All alloys were sealed in quartz tubes and annealed at 900 °C for 100 h before quenching in cold

water. X-ray powder diffraction data from as-cast and annealed alloys were collected on a Guinier-Huber image plate system with Cu $K\alpha 1$ ($8 < 2\Theta < 100°$). Refinement of the crystal structures was performed with the program FULLPROF.[19] Measurements of the various physical properties were carried out with a series of standard techniques.[20]

III. COMPUTATIONAL ASPECTS

The density-functional theory (DFT) calculations were done by using the Vienna *ab initio* simulation package (VASP) utilizing the projector augmented wave construction for the pseudopotentials.[21] The potential for Ba comprises 10 valence states including the 5*s* and 5*p* (semi)core states, whereas for Pt and Si the standard number of valence states of 10 and 4, respectively, are included. For the approximation of the exchange-correlation functional a local density approach (LDA) was preferred over a generalized gradient approximation (GGA) because of the heavy elements Ba and Pt. Comparisons of GGA and LDA results revealed that the typical underestimation of the volume by LDA is smaller than the corresponding overestimation by the GGA treatment. The size of the basis set was defined by an energy cutoff of 500 eV. The radii (in Å) as chosen for the atom projections of the density of states (DOS) are 1.98 for Ba, 1.30 for Pt, and 1.11 for Si. Relativistic spin-orbit (SO) coupling was included in a self-consistent manner. The structural parameters (lattice parameters as well as atomic positions) were optimized by total energy as well as force minimization within the SO application. For the Brillouin zone integration a tetrahedron interpolation for 216 $\vec{k}$ points in the irreducible part of the Brillouin zone was used. Vibrational properties in terms of phonon dispersions and the corresponding density of states were calculated within the direct phonon approach.[22]

IV. RESULTS AND DISCUSSION

A. Crystal chemistry

The crystal structure was determined from x-ray Rietveld refinement and found to be a tetragonal, noncentrosymmetric structure, corresponding to the space group *I*4*mm*, which is isotypic to $BaNiSn_3$ (as shown in Fig. 1) being an ordered variant of the centrosymmetric $ThCr_2Si_2$ structure type. The tetragonal crystallographic (standardized) data are: $a = 0.44094(2)$nm and $c = 1.0013(3)$nm; Ba is at the 2(a) site with coordinates 0, 0, and 0.6022(8); Pt at the 2(a) site with 0, 0, and 0.2502(7); Si(2) at the 2(a) site with 0, 0, and 0; and Si(1) at the 4(b) site with 0, 0.5, and 0.3608(8).

B. Superconductivity

Measurements of the temperature-dependent electrical resistivity of $BaPtSi_3$ were carried out from 400 mK to room temperature, and the results are shown in Fig. 2. The superconducting transition occurs at $T_c \approx 2$ K below which the resistivity vanishes.

The resistivity in the normal-state region for temperatures $T > T_c$ corresponds to a metal and can be described by the

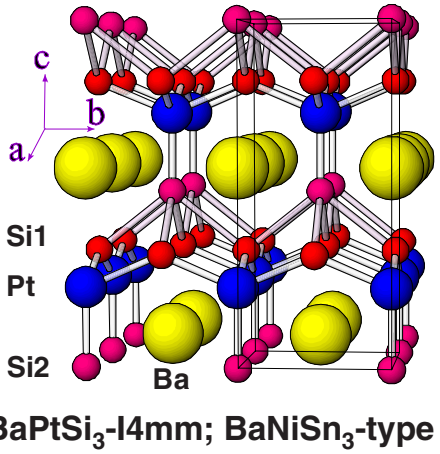

FIG. 1. (Color online) Sketch of the crystal structure of $BaPtSi_3$. Note the loss of centrosymmetry due to the arrangement of Pt and Si atoms.

Bloch-Grüneisen model. The least squares fit is shown as a dashed line in Fig. 2 resulting in a Debye temperature of $\theta_D = 345$ K. An estimation of the strength of the electron-phonon interaction can be derived in terms of the McMillan formula.[23] McMillan's model contains the dimensionless electron-phonon coupling constant λ, which is—in terms of the Eliashberg theory—related to the phonon density of states. The parameter λ determines the attractive part of the Cooper pair bonding, while the parameter μ^* represents the repulsive screened Coulomb part, which is usually set to ≈ 0.13. Applying this simple model for $BaPtSi_3$ yields a value of $\lambda \approx 0.5$ characterizing a superconductor in the weak-coupling limit.

The application of a magnetic field (see inset in Fig. 2) rapidly suppresses superconductivity already at fields of a few tenth of a tesla. A reduction in the superconducting transition temperature by an initial rate of −0.06 K/kbar [inset in Fig. 2(b)] follows from the pressure-dependent measurements of the electrical resistivity [shown in Fig. 2(b)]. If the Debye temperature remains constant under pressure, the flattening of features of the electronic density of states at the Fermi energy upon application of pressure results then in a decrease in T_c,[24] as observed for the vast majority of BCS superconductors.

Figure 3 shows the heat capacity of $BaPtSi_3$ below ≈ 100 K, plotted in terms of C_p/T vs T. A standard low-temperature approximation of the heat-capacity data yields a Sommerfeld value of $\gamma \approx 5.7$ mJ/mol K^2, while extended temperature ranges with a pronounced T^3 dependence of the specific heat are missing. The absence of a maximum in the C_p/T curve below 100 K, however, refers to a rather large Debye temperature on the order of at least 350 K. In fact, a simple Debye function, $C_D(T)$, when plotted as C_D/T vs T yields a global maximum for $\theta_D \approx 3.6$ T(C_p/T[max]). At low temperatures, a small anomaly becomes evident; in agreement with our resistivity data, bulk superconductivity around 2 K can be concluded. Details of the superconducting transition are compiled in the inset of Fig. 3.

Idealizing the specific-heat jump to ensure entropy balance, the superconducting transition temperature can be de-

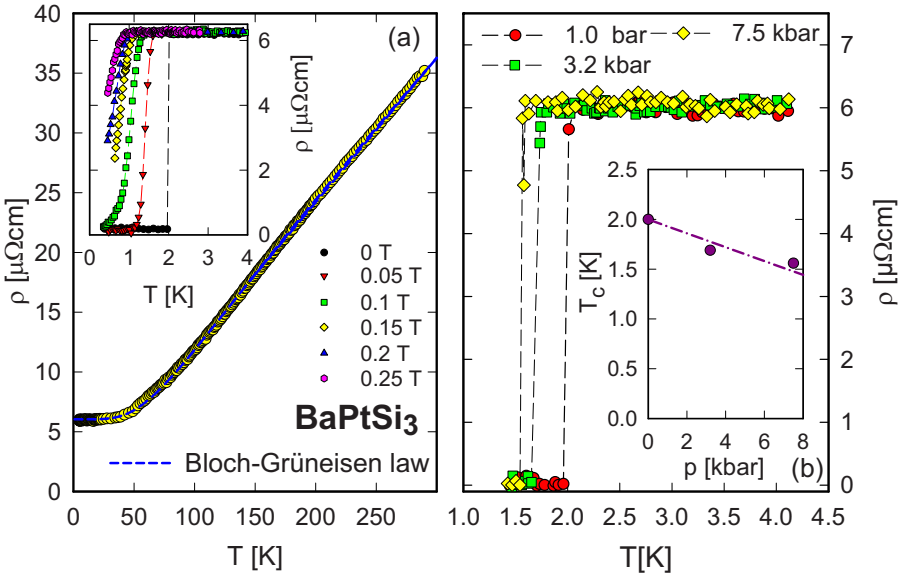

FIG. 2. (Color online) Panel (a) shows the temperature-dependent electrical resistivity ρ of $BaPtSi_3$. The dashed line denotes a least-squares fit according to the Bloch-Grüneisen law resulting in the Debye temperature of $\theta_D=345$ K. The inset shows the field response of the superconducting transition as measured at various externally applied magnetic fields. Panel (b) shows the temperature-dependent electrical resistivity ρ of $BaPtSi_3$ measured at various applied pressures. The inset shows the pressure dependence of the superconducting transition temperature T_c, initially varying as $\partial T_c/\partial p=-0.06$ K/kbar.

termined as $T_c=2.25$ K (inset in Fig. 3, vertical dashed line). The idealized anomaly of the heat capacity $\Delta C_p/T(T=T_c) \approx 7.8$ mJ/mol K^2 results in the estimation of $\Delta C_p/(\gamma_n T_c) \approx 1.38$, which is close to the BCS value of $\Delta C_p/(\gamma T_c) \approx 1.43$. Furthermore, the BCS-type superconductivity follows directly from the temperature dependence of the specific heat $C_p(T)$ in the superconducting state. The solid line in the inset of Fig. 3 models $C_p(T)$ by applying the generalized BCS dataset of Mühlschlegel,[25] which is done without any adjustable parameter. Except for the very low-temperature range below 500 mK, an almost perfect agreement between the theoretical estimation and experiment is observed, emphasizing a BCS-type superconductivity corresponding to spin-singlet pairing and a fully gapped electronic density of states right at the Fermi energy. The discrepancy observed in the heat-capacity data at very low temperatures may either be due to measurement problems or due to a tiny impurity effect: the maximum contribution around 250 mK is only 1 mJ/mol K^2. The application of external fields rapidly suppresses bulk superconductivity; accordingly, a field of 0.01 T shifts T_c by about 0.25 K to lower temperatures, while fields on the order of 0.05 T obviously inhibit superconductivity. Thus, the initial slope of the upper critical field $\mu_0 H'_{c2}(T)$ results in a value of −0.033 T/K, which is substantially lower than the value deduced from the resistivity data according to $\mu_0 H'_{c2}(T) \approx -0.1$ T/K.

Superconductivity in terms of the BCS model relies on the coupling of electrons to lattice vibrations. Thus, the knowledge of the lattice dynamics is of importance. An estimation of relevant phonon branches can be derived from the specific-heat data analyzed in terms of a model suggested by Junod *et al.*[26,27] In this model, the temperature-dependent quantity $(C_p-\gamma T)/T^3$ allows a straightforward inspection of deviations from the simple Debye model. The model phonon spectrum, however, consists of a Debye spectrum overlaid by Einstein branches with finite spectral widths, according to Ref. 28. The experimental data for $BaPtSi_3$ are shown in Fig. 4, referring to the left axis of this graph. As already mentioned, there are significant deviations from the Debye model as shown by the dotted line in Fig. 4, justifying the inclusion of optical branches in terms of two Einstein-type contributions. A least-squares fit according to Junod's model reveals a phonon spectrum $F(\omega)$ represented by the dotted lines in Fig. 4 yielding a Debye temperature $\theta_D=370$ K, as well as

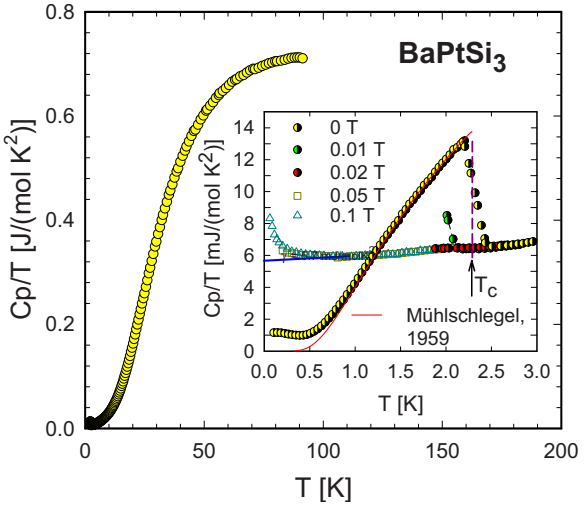

FIG. 3. (Color online) Temperature-dependent specific heat C_p of $BaPtSi_3$, plotted as C_p/T vs T. The inset shows low-temperature details of the superconducting transition for various values of externally applied magnetic fields. The solid line represents the temperature-dependent specific heat of a spin-singlet fully gapped superconductor according to the model of Mühlschlegel, Ref. 25.

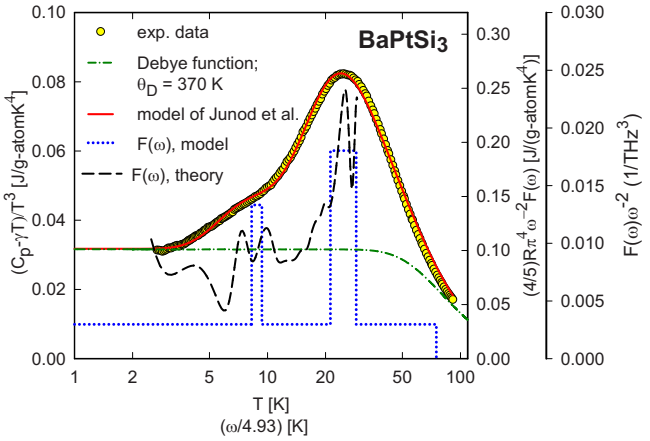

FIG. 4. (Color online) Temperature-dependent specific heat C_p of $BaPtSi_3$, plotted as $(C_p-\gamma T)/T^3$ vs ln T. The solid line is a least-squares fit of the experimental data using the model described in the text and the dashed-dotted line represents a simple Debye contribution with θ_D=370 K. The essential parameters of the model used to construct the spectral function $F(\omega)$ (dotted lines, right axis), are θ_D=370 K, ω_{E1}=43 K with a width of 5.3 K and ω_{E2}=128 K with a width of 37 K. The DFT derived function $F_{\mathrm{DFT}}(\omega)/\omega^2$ (F_{DFT} being the phonon density of states as calculated by DFT) is shown as a dashed line, referring to the second axis on the right-hand side.

the Einstein modes ω_{E1}=43 K and ω_{E2}=128 K with frequency widths $\Delta\omega$ of 5 and 37 K, respectively. The corresponding spectral weights of these contributions are 9, 0.5, and 5.5 for the Debye, the Einstein (1), and the Einstein (2) modes, respectively. It may be speculated that the low-lying phonon branches at 43 K are involved in the formation of Cooper pairs. The Debye temperature deduced from this model almost perfectly coincides with the value as derived from the resistivity fit. The function $F_{\mathrm{DFT}}(\omega)/\omega^2$, where F_{DFT} is the phonon density of states as calculated by DFT (see

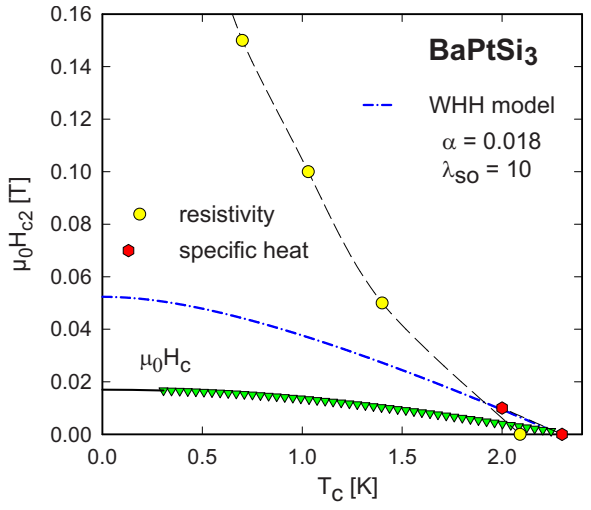

FIG. 5. (Color online) Temperature-dependent upper critical field $\mu_0 H_{c2}$ and thermodynamic critical field $\mu_0 H_c$ of $BaPtSi_3$ as obtained from resistivity and specific-heat measurements. The dashed-dotted line represents the WHH model. The solid line is an extrapolation of the thermodynamic critical field towards zero and the dashed line serves as a guide to the eyes.

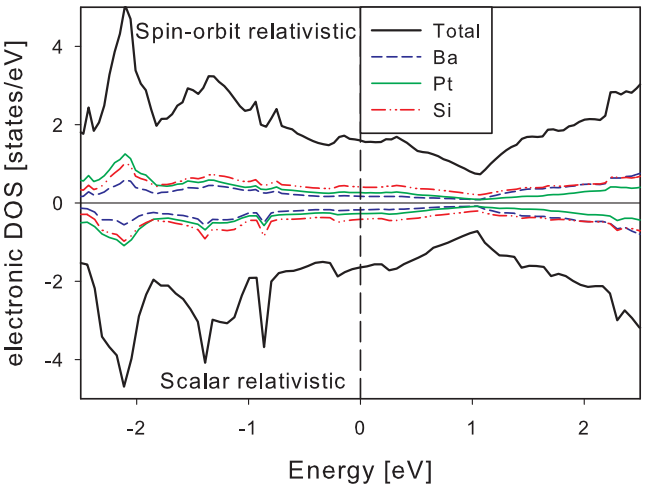

FIG. 6. (Color online) Section of total and atom-projected densities of states (DOS; in states eV^{-1}) for $BaPtSi_3$ in the energy range $\pm$2.5 around the Fermi energy E_F. Energy scale is defined relative to E_F. Upper panel: DOS with SO coupling; lower panel: DOS for scalar relativistic calculation. Total DOS (solid lines) split into Ba like (dotted lines), Pt like (dashed-dotted lines), and Si like (dashed lines) DOS summed over all three Si atoms.

below), is shown as a dashed line, demonstrating the usefulness of the model put forward by Junod *et al.*[26,27]

Figure 5 reveals the temperature-dependent upper critical field values $\mu_0 H_{c2}$ for $BaPtSi_3$ as obtained from both resistivity and specific-heat data. As already mentioned, these values are different, most likely due to surface effects in the resistivity data, giving rise to a critical field $H_{c3}(T)$. [Note that in the simplest models, $H_{c3}(T) \approx 1.7 H_{c2}(T)$, Ref. 29.] Werthamer *et al.*[30] derived an expression [abbreviated as Werthamer, Hefland, and Hohenberg (WHH) model] for the upper critical field $\mu_0 H_{c2}$ in terms of orbital pair breaking, including the effect of Pauli spin paramagnetism and spin-orbit scattering. The WHH model is based on two parameters, namely, α, the Pauli paramagnetic limitation or Maki parameter, and λ_{so} which describes spin-orbit scattering. While the value of α allows a rough discrimination between orbital pair breaking and Pauli limiting, λ_{so} is dominated by the atomic numbers of the elements of the material under consideration.

The Maki parameter α can be estimated[30] from the Sommerfeld value γ and ρ_0 via the expression $\alpha = (3e^2\hbar\gamma\rho_0)/(2m\pi^2 k_B^2)$ in which e denotes the charge and m the mass of an electron. Considering the experimental values for ρ_0 and γ results in a value of α=0.018. A value for α of similar magnitude can be derived from the expression $\alpha = 5.3\times10^{-5}\left(\frac{-dH_{c2}(T)}{dT}\right)\Big|_{T=T_c} = 0.017$.[31] The very low value of α clearly indicates that orbital pair breaking is the essential mechanism, which limits the upper critical field.

The overall temperature dependence of the upper critical field $\mu_0 H_{c2}$ as derived from the WHH model is displayed by a dashed-dotted line in Fig. 5, revealing the value $\mu_0 H_{c2}(0)$ =0.053 T at $T\to0$, which is in very good agreement to the low-temperature specific-heat data. The thermodynamical critical field is calculated from the free-energy difference between the superconducting and normal states, which

is given by the expression $\Delta F(T)=F_n-F_s=\mu_0 H_c^2(T)/2 = \int_{T_c}^{T}\int_{T_c}^{T'}\frac{(C_s-C_n)}{T''}dT''dT'$. The quantity $C_s(T)$ is obtained from the zero-field specific-heat measurement whereas $C_n(T)$ is obtained from the data corresponding to 0.1 T. The derived values are marked in Fig. 5 by shaded triangles; an extrapolation to $T\rightarrow 0$ yields an estimation of $\mu_0 H_c(0)\approx 0.018$ T.

In the scope of the BCS theory, various microscopic parameters can be calculated from superconducting and normal-state properties,[32] by taking into account $\gamma = 5.8$ mJ/mol K^2, $\mu_0 H'_{c2}=-0.033$ T/K, $\mu_0 H_{c2}(0)= -0.053$ T, and $\rho_0=6$ $\mu\Omega$ cm. The effective Fermi surface S_s is computed (Ref. 33) as $S_s^{cl}\simeq 3\times 10^{20}$ m^{-2} within the clean and $S_s^{dl}\simeq 1.2\times 10^{21}$ m^{-2} for the dirty limit. Considering the dirty limit only, the calculated $\mu_0 H'_{c2}(\text{calc})=-0.026$ T/K is in fine agreement with the experimentally derived slope. Combining the Fermi surface with γ yields the Fermi velocity $v_F\simeq 162000$ m/s, and in the context of the residual resistivity, $\rho_0=6$ $\mu\Omega$ cm, a mean free path $l_{tr}\simeq 7.7\times 10^{-8}$ m can be derived. The coherence length ξ_0 for $T\rightarrow 0$ was obtained from two independent relations. One follows from the BCS equation, $\xi_0=0.18\hbar v_F/(k_B T_c)\simeq 9.9\times 10^{-8}$ m. A second expression stems from the well-known formula $\mu_0 H_{c2} =\Phi_0/(2\pi\xi_0^2)$, yielding $\xi_0\simeq 7.9\times 10^{-8}$ m, in fair agreement with the former. The thermodynamical critical field $\mu_0 H_c$ follows from $\gamma T_c^2=0.168\mu_0 H_c^2$, thus $\mu_0 H_c\simeq 0.017$ T, in perfect analogy with the experimental result. With the estimate $H_{c2}(0)\approx 0.053$ T one derives a value for the dimensionless Ginzburg Landau parameter $\kappa_{GL}=H_{c2}(0)/(\sqrt{2}H_c)\simeq 2.2$ which, in turn, determines the London penetration depth $\lambda_L(T\rightarrow 0)\simeq 2.6\times 10^{-7}$ m. Based on the estimate $l_{tr}/\xi\approx 0.1$ we classify $BaPtSi_3$ as a superconductor in the dirty limit, and the value of $\kappa_{GL}\approx 2$ refers to a type II superconductor.

V. DFT ELECTRONIC STRUCTURE

A section of the calculated electronic DOS of $BaPtSi_3$ is shown in Fig. 6, for both a nonrelativistic (lower panel) and relativistic (including spin-orbit coupling) calculations (upper panel). The main difference between these two calculations occurs at about −1.5 eV below the Fermi energy, at which energies the scalar relativistic DOS splits into two prominent peaks of mixed Pt d and Si p character. The spin-orbit coupling most strongly affects the Pt-like states, which—due to hybridization—transfer the relativistic effect to the Si-like states. The states at the Fermi level are mainly composed of Si p and Pt $5d$ states, as well as a smaller contribution from Ba p states. Hybridization is clearly indicated by local DOS features, which are common to all three atom-projected DOS contributions. Close to the Fermi energy, E_F, both calculations produce very similar and rather smooth DOS features. None of the DOS exhibit significant features around E_F, indicating good metallic behavior. The values of the total DOS at E_F are $N(E_F)=1.64$ and 1.60 states eV^{-1} for the SO and scalar relativistic calculation, respectively. Within the lowest order Sommerfeld expansion for the electronic specific heat C_e, the derived values for γ [$\gamma = \frac{\pi^2}{3}k_B N(E_F)$ as defined by $C_e=\gamma T$] are 3.9 and 3.8 mJ/mol K^2, respectively. Considering the experimentally estimated value for the normal state, $\gamma = 5.8$ mJ/mol K^2, a phonon enhancement factor of 1.5 is obtained, which is a reasonable value for a weak-coupling BCS superconductor. Moreover, it perfectly matches the value as derived via the McMillan model.

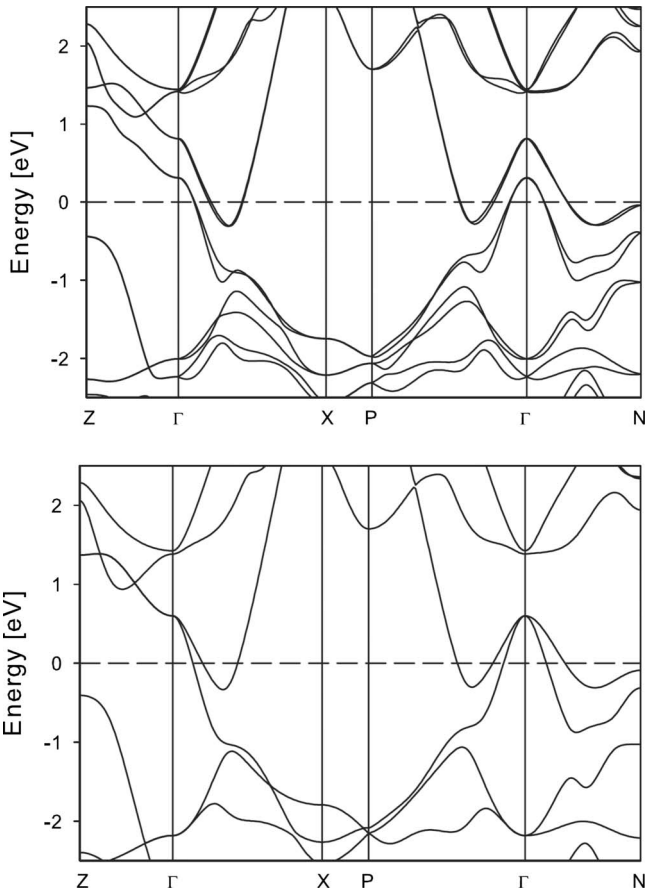

FIG. 7. Section of electronic band structure along high symmetry directions for $BaPtSi_3$ in the energy range ±2.5 around the Fermi energy E_F. Upper panel: spin-orbit coupling included; lower panel: scalar relativistic only. Brillouin zone, see Fig. 8.

Figure 7 shows the electronic band structure with SO coupling (upper panel) and without (lower panel). Switching on SO, the symmetry of bands is reduced and degeneracies of scalar-relativistic bands are lifted, as can be seen at the Γ point about 0.6 eV above E_F: the degenerate scalar-relativistic state (lower panel) splits into two states in the SO case (upper panel) with a sizeable splitting of 0.5 eV. This particular state is of Pt d character, and—because of the high nuclear charge of Pt—the SO effect is significant. A further symmetry effect is the splitting of each of the SO bands into two subbands (upper panel), which is due to the missing inversion symmetry in real space. Focussing on bands near Fermi energy, two sets of bands start at Γ with energies of 0.31 eV (bands 1,2) and 0.81 eV (bands 3,4). These bands cross the Fermi energy in directions Γ-X, Γ-P, and Γ-N. Because bands 3,4 change their directions and turn around, they cross two times the Fermi energy along Γ-N and Γ-P. According to Fig. 7 the splitting of the bands crossing E_F is rather small. However, studying the bands along other directions such as the in-plane directions [100] and [010] reveals

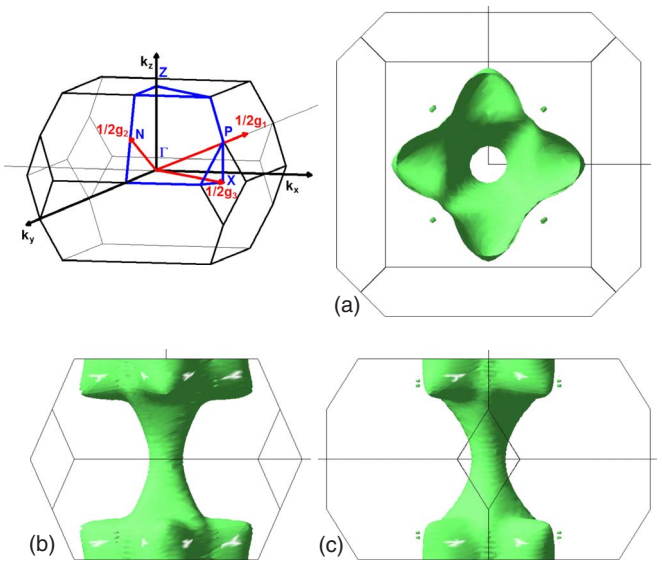

FIG. 8. (Color online) Fermi surface of band 1 (see text). (a) view in direction Z-Γ; (b) view in direction [100]; (c) view in direction X-Γ. Top left panel: Brillouin zone of the body-centered tetragonal lattice for $c > a$.

a sizeable splitting of about 0.3 eV for bands 1 and 2 which recross E_F. These bands, however, result in very small isolated Fermi surfaces [compare Figs. 8(a) and 8(c)]. A very important observation is that no band crosses E_F along [001] (direction Γ-Z). This is directly reflected in the shape of the Fermi surfaces: they are either of dumbbell or of toruslike shapes with the c axis as rotation axis (see Figs. 8 and 9). The three views of the Fermi surface of bands 1 and 2 (see Fig. 8) show a peculiar narrow funnel-shaped tube with its axis along Γ-Z, presumably illustrating (rather isotropic) nesting features corresponding to rather short $\vec{k}$ vectors. Because of the discussed rather small band splittings due to the

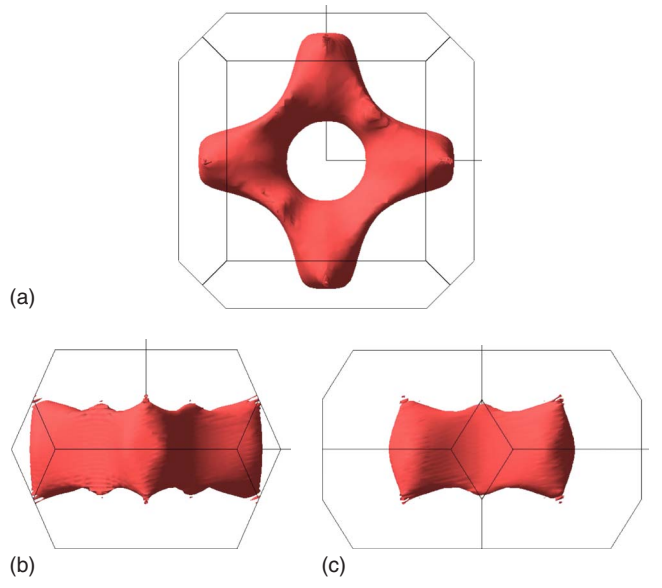

FIG. 9. (Color online) Fermi surface of band 4 (see text). (a) view in direction Z-Γ; (b) view in direction [100]; and (c) view in direction X-Γ.

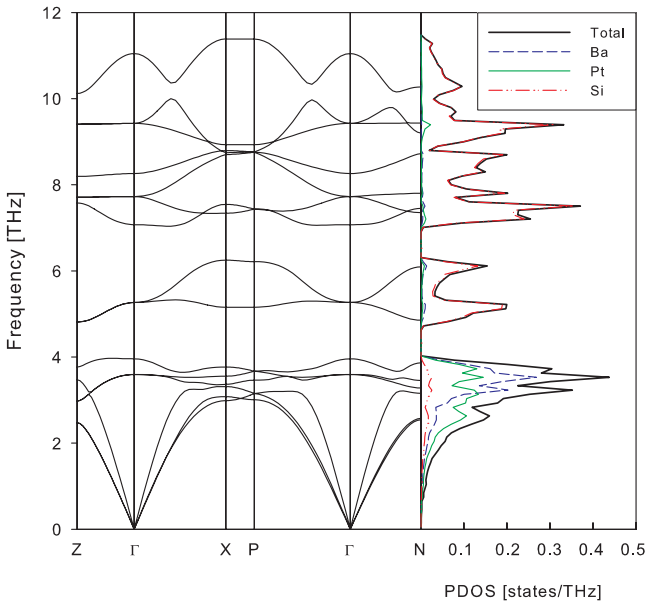

FIG. 10. (Color online) DFT-derived phonon dispersions and density of states. The PDOS is split into contributions of local modes attributed to Ba, Pt, and Si atoms.

missing inversion symmetry, the Fermi surface of band 2 is very similar to band 1 and is therefore not shown. Concerning band 4 (Fig. 9), nesting can be imagined between parallel surfaces in adjacent Brillouin zones, as illustrated by the side views in the figure. These surfaces shape the outer side of the torus. The corresponding nesting vector, however, is significantly larger than for bands 1 and 2. Again, because of the rather small band splittings the Fermi surface of band 3 is very similar to its counterpart of band 4, and is therefore not shown. Finally, two additional bands below bands 1,2 form very thin ringlike Fermi surfaces (not shown here).

VI. DFT PHONONS

Figure 10 presents phonon dipersions along high symmetry directions in $\vec{q}$ space, as well as the phonon density of states (PDOS). The PDOS F_{DFT} is split into contributions of local atomic modes showing that the low-frequency vibrational spectrum up to 4 THz is dominated by the heavy atoms Ba and Pt. At higher frequencies the two well-separated PDOS features between 5 and 6 THz, and above 7 THz can be attributed almost exclusively to Si. According to analysis of the experimental specific heat (see Fig. 4 and the accompanying discussion) two Einstein-type modes are extracted, which correspond to frequencies of $\omega_{E1} \approx 1$ THz and $\omega_{E2} \approx 2.6$ THz. The larger frequency mode coincides with the lowest Einstein-type modes of the DFT phonon spectrum in Fig. 10, which is illustrated in Fig. 4 by showing $F_{\mathrm{DFT}}(\omega)/\omega^2$. At the lower frequency ω_{E1} at which the formation of Cooper pairs is suspected (see discussion in Sec. IV B) the function $F_{\mathrm{DFT}}(\omega)/\omega^2$ exhibits a peaklike feature indicating a significant deviation from Debye's model.

From the phonon dispersions it can be estimated that at 1 THz the corresponding $\vec{q}$ values would correspond rather well to the diameter of the hollow funnel-shaped dumbbells

formed by the Fermi surfaces of bands 1 and 2 according to Fig. 8, indicating the coincidence of unusual phonon modes with electronic nesting features. Similar features have been observed for $BaPtGe_3$. Details will be the subject of a forthcoming paper.[34]

VII. SUMMARY

$BaPtSi_3$ is a new noncentrosymmetric compound. Specific-heat and electrical resistivity studies characterize $BaPtSi_3$ as a superconductor with T_c=2.25 K. All experimental parameters and analyses point to a BCS-like superconductivity, which is based on spin-singlet pairing with a fully gapped DOS at E_F. $BaPtSi_3$ is classified as a type II superconductor in the dirty limit. The absence of inversion in the crystal structure is suggested to give rise to anomalous features of the superconducting state such as a mixing of spin-singlet and spin-triplet pairs, as well as nodes in the superconducting gap at the Fermi surface.[35,36] Although our electronic-structure calculations evidence a splitting of bands due to spin-orbit interactions, the overall effect of noninversion symmetry seems to be of minor importance for the superconducting properties. In this respect, $BaPtSi_3$ seems to be in line with conclusions drawn for Li_2Pd_3B.[14]

ACKNOWLEDGMENTS

Work was supported by the Austrian Science Foundation FWF under Projects No. P18054 and No. P18480, as well as by the COST P16 program.

[1] E. Bauer, G. Hilscher, H. Michor, Ch. Paul, E. W. Scheidt, A. Gribanov, Yu. Seropegin, H. Noël, M. Sigrist, and P. Rogl, Phys. Rev. Lett. **92**, 027003 (2004).
[2] T. Akazawa, H. Hidaka, T. Fujiwara, T. C. Kobayashi, E. Yamamoto, Y. Haga, R. Settai, and Y. Onuki, J. Phys.: Condens. Matter **16**, L29 (2004).
[3] N. Kimura, K. Ito, K. Saitoh, Y. Umeda, H. Aoki, and T. Terashima, Phys. Rev. Lett. **95**, 247004 (2005).
[4] I. Sugitani, Y. Okuda, H. Shishido, T. Yamada, A. Thamizhavel, E. Yamamoto, T. D. Matsuda, Y. Haga, T. Takeuchi, R. Settai, and Y. Onuki, J. Phys. Soc. Jpn. **75**, 043703 (2006).
[5] L. P. Gor'kov and E. I. Rashba, Phys. Rev. Lett. **87**, 037004 (2001).
[6] C. Krupka, A. L. Giorgi, N. H. Krikorian, and E. G. Szklarz, J. Less-Common Met. **19**, 113 (1969).
[7] A. L. Giorgi, E. G. Sklarz, N. H. Krikorian, and M. C. Krupka, J. Less-Common Met. **22**, 131 (1970).
[8] G. Amano, S. Akutagawa, T. Muranaka, Y. Zenitani, and J. Akimitsu, J. Phys. Soc. Jpn. **73**, 530 (2004).
[9] M. Hanawa, Y. Muraoka, T. Tayama, T. Sakakibara, J. Yamaura, and Z. Hiroi, Phys. Rev. Lett. **87**, 187001 (2001).
[10] H. Sakai, K. Yoshimura, H. Ohno, H. Kato, S. Kambe, R. E. Walstedt, T. D. Matsuda, Y. Haga, and Y. Onuki, J. Phys.: Condens. Matter **13**, L785 (2001).
[11] K. Togano, P. Badica, Y. Nakamori, S. Orimo, H. Takeya, and K. Hirata, Phys. Rev. Lett. **93**, 247004 (2004).
[12] P. Badica, T. Kondo, and K. Togano, J. Phys. Soc. Jpn. **74**, 1014 (2005).
[13] M. Nishiyama, Y. Inada, and G.-q. Zheng, Phys. Rev. B **71**, 220505(R) (2005).
[14] H. Q. Yuan, D. F. Agterberg, N. Hayashi, P. Badica, D. Vandervelde, K. Togano, M. Sigrist, and M. B. Salamon, Phys. Rev. Lett. **97**, 017006 (2006).
[15] K. W. Lee and W. E. Pickett, Phys. Rev. B **72**, 174505 (2005).
[16] P. S. Häfliger, R. Khasanov, R. Lortz, A. Petrović, K. Togano, C. Baines, B. Graneli, and H. Keller, J. Supercond. Novel Magn. **22**, 337 (2009).
[17] E. Bauer, H. Kaldarar, R. Lackner, H. Michor, W. Steiner, E.-W. Scheidt, A. Galatanu, F. Marabelli, T. Wazumi, K. Kumagai, and M. Feuerbacher, Phys. Rev. B **76**, 014528 (2007).
[18] N. Melnychenko-Koblyuk, A. Grytsiv, P. Rogl, E. Bauer, R. Lackner, E. Royanian, M. Rotter, G. Giester, J. Phys. Soc. Jpn. **77**, Supplement A, 54 (2008).
[19] T. Roisnel and J. Rodríguez-Carvajal, Mater. Sci. Forum **378-381**, 118 (2001).
[20] E. Bauer, St. Berger, Ch. Paul, M. Della Mea, G. Hilscher, H. Michor, M. Reissner, W. Steiner, A. Grytsiv, P. Rogl, and E. W. Scheidt, Phys. Rev. B **66**, 214421 (2002).
[21] G. Kresse and J. Furthmüller, Phys. Rev. B **54**, 11169 (1996); G. Kresse and D. Joubert, *ibid.* **59**, 1758 (1999).
[22] K. Parlinski, PHONON 4.25, 2005, as implemented in MEDEA, Materials Design Inc., www.materialsdesign.com; K. Parlinski, Z.-Q. Li, and Y. Kawazoe, Phys. Rev. Lett. **78**, 4063 (1997).
[23] W. L. McMillan, Phys. Rev. **167**, 331 (1968).
[24] N. N. Bogoljubov, V. V. Tolmachov, and D. V. Širkov, Fortschr. Phys. **6**, 605 (1958).
[25] B. Mühlschlegel, Z. Phys. **155**, 313 (1959).
[26] A. Junod, D. Bichsel, and J. Muller, Helv. Phys. Acta **52**, 580 (1979).
[27] A. Junod, T. Jarlborg, and J. Muller, Phys. Rev. B **27**, 1568 (1983).
[28] St. Berger, Ph.D. thesis, TU Wien, 2003.
[29] M. Tinkham, *Introduction to Supercondcutivity* (McGraw-Hill, New York, 1975).
[30] N. R. Werthamer, E. Hefland, and P. C. Hohenberg, Phys. Rev. **147**, 295 (1966).
[31] K. Maki, Phys. Rev. **148**, 362 (1966).
[32] T. P. Orlando, E. J. McNiff, Jr., S. Foner, and M. R. Beasley, Phys. Rev. B **19**, 4545 (1979).
[33] U. Rauchschwalbe, Physica B & C **147**, 1 (1987).
[34] E. Bauer, R. T. Khan, H. Michor, E. Royanian, A. Grytsiv, P. Rogl, D. Reith, R. Podloucky, E. W. Scheidt, W. Wolf, and M. Marsman (unpublished).
[35] P. A. Frigeri, D. F. Agterberg, A. Koga, and M. Sigrist, Phys. Rev. Lett. **92**, 097001 (2004).
[36] N. Hayashi, K. Wakabayashi, P. A. Frigeri, and M. Sigrist, Phys. Rev. B **73**, 092508 (2006).